ARTICLE

Bimetallic NiCo$_2$S$_4$ Nanoneedles Anchored on Mesocarbon Microbeads as Advanced Electrodes for Asymmetric Supercapacitors

Yu Zhang[1], Yihe Zhang[1] ✉, Yuanxing Zhang[1], Haochen Si[1], Li Sun[1] ✉

✉ Yihe Zhang, zyh@cugb.edu.cn; Li Sun, sunli@cugb.edu.cn

[1] Beijing Key Laboratory of Materials Utilization of Nonmetallic Minerals and Solid Wastes, National Laboratory of Mineral Materials, School of Materials Science and Technology, China University of Geosciences, Beijing 100083, People's Republic of China
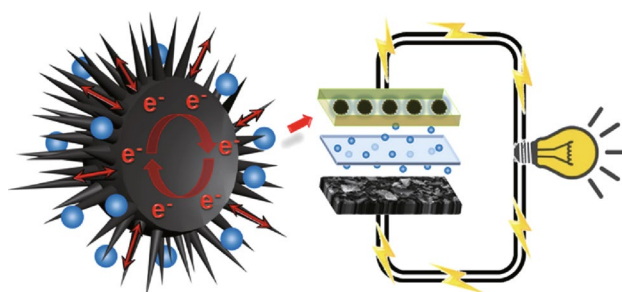
HIGHLIGHTS

- A facile method was used to anchor pseudocapacitive bimetallic NiCo$_2$S$_4$ (NCS) nanoneedles on mesocarbon microbeads (MCMBs), forming a novel urchin-like structure.

- The NCS@MCMB electrode and an assembled asymmetric supercapacitor displayed good electrochemical performance.

ABSTRACT Bimetallic Ni–Co sulfides are outstanding pseudocapacitive materials with high electrochemical activity and excellent energy storage performance as electrodes for high-performance supercapacitors. In this study, a novel urchin-like NiCo$_2$S$_4$@mesocarbon microbead (NCS@MCMB) composite with a core–shell structure was prepared by a facile two-step hydrothermal method. The highly conductive MCMBs offered abundant adsorption sites for the growth of NCS nanoneedles, which allowed each nanoneedle to fully unfold without aggregation, resulting in improved NCS utilization and efficient electron/ion transfer

in the electrolyte. When applied as an electrode material for supercapacitors, the composite exhibited a maximum specific capacitance of 936 F g^{-1} at 1 A g^{-1} and a capacitance retention of 94% after 3000 cycles at 5 A g^{-1}, because of the synergistic effect of MCMB and NCS. Moreover, we fabricated an asymmetric supercapacitor based on the NCS@MCMB composite, which exhibited enlarged voltage windows and could power a light-emitting diode device for several minutes, further demonstrating the exceptional electrochemical performance of the NCS@MCMB composite.

KEYWORDS Bimetallic sulfides; NiCo$_2$S$_4$; Nanoneedles; Mesocarbon microbeads; Asymmetric supercapacitor

1 Introduction

In the last few decades, the growing demand for high-performance mobile devices and renewable energy has promoted the continuous development of energy storage devices [1–5]. Supercapacitors have shown potential applications in energy storage, owing to their high power density, short charge–discharge time, long cycle life, and environmental friendliness [6–14]. The electrochemical performance of supercapacitors is strongly dependent on the electrode materials, which is also the key element for overcoming the limited energy density issues affecting supercapacitors. From the viewpoint of electrochemical performance, an ideal electrode material is expected to provide high

specific capacitance and outstanding electrochemical stability. Despite their high electrical conductivity and long cycle life, traditional carbon materials exhibit capacitances based on the electrochemical double-layer capacitor (EDLC) mechanism; therefore, they cannot provide the large energy densities required by advanced energy devices [15–17]. In comparison, the specific capacitance of pseudocapacitive materials such as conducting polymer and transition metal compounds generally originates from reversible redox reactions; therefore, these materials can provide larger specific capacitances and higher energy densities [18–24].

Transition metal sulfides, especially bimetallic Ni–Co sulfides, have recently attracted considerable scientific and technological interest due to their excellent electrochemical performance [25–29]. On the one hand, these materials possess higher electrical conductivity, due to their lower band gap than that of ternary Ni–Co oxides [30–32]. On the other hand, the Ni–Co sulfides show richer Faradaic redox reactions than monometallic sulfides [33, 34], due to the contribution from the bimetallic elements, which results in higher specific capacitances [35–38]. However, similar to most other pseudocapacitive materials, the intrinsically low electronic conductivity, irreversible redox reactions, and structural instability of Ni–Co sulfides often limit their rate capability and cycle life after repeated Faradaic redox reactions [39, 40]. Although various bimetallic Ni–Co sulfides with different morphologies and components have been explored, their electronic conductivity and structural stability during long-term cycling are still unsatisfactory. To overcome these drawbacks, various carbonaceous materials were considered as hosts to load active materials and prepare composites. Several advantageous features have been identified for these carbon–NCS composites, including a highly open structure based on their carbon framework, an improved electrical conductivity of the electrode, an enhanced utilization of the active material, and a reduced dissolution of active materials into electrolytes. Compared to the widely used carbon nanotubes [41–44] and graphene [45–48], mesocarbon microbead (MCMB) materials are regarded as promising carbon hosts due to their low cost and easy synthesis, which are favorable for large-scale applications. The high conductivity of MCMB is expected to enhance the overall electrical conductivity of the composite, thus resulting in an improved electron transfer during electrochemical reactions. The spherical and open structure of MCMB can also provide a large number of adsorption sites to anchor other materials,

which would enable a high loading of active materials. In addition, the robust solid structure of MCMB can produce a highly stable composite without massive agglomeration during electrochemical reactions, leading to a high structural stability of the electrode.

In this work, we adopted a facile two-step hydrothermal method to prepare a novel $NiCo_2S_4$@MCMB composite with urchin-like core–shell structure, by directly growing $NiCo_2S_4$ (NCS) nanoneedles on MCMBs. When evaluated as an electrode material for supercapacitors, the as-prepared NCS@MCMB composite displayed satisfactory electrochemical performance, which was attributed to its stable and open urchin-like structure. Moreover, the NCS@MCMB composite was also tested as an electrode material of asymmetric supercapacitors (ASCs), further confirming its potential in practical applications such as energy storage devices.

2 Experimental Section

2.1 Material Preparation

2.1.1 Synthesis of NCS@MCMB Precursors

The MCMB reactant was an industrial product prepared from coal tar pitch. The composites were synthesized by a facile two-step hydrothermal process: 101.6 mg of MCMB was first dispersed in 40 mL of deionized water by ultrasonication for 30 min, to obtain a suspension. Then, 1 mmol of $Ni(NO_3)_2 \cdot 6H_2O$, 2 mmol of $Co(NO_3)_2 \cdot 6H_2O$, and 12 mmol of urea were dissolved into the well-dispersed MCMB suspension, and the mixture was stirred for 20 min to obtain a clear dark pink solution. The suspension was placed into a 50-mL Teflon-lined stainless steel autoclave and maintained at 120 °C for 8 h. After cooling down to room temperature, the precipitate was collected and washed several times with deionized water and ethanol, followed by drying at 60 °C for 24 h in vacuum prior to the subsequent hydrothermal process.

2.1.2 Synthesis of NCS@MCMB

$Na_2S \cdot 9H_2O$ (1.17 g) was dissolved in 40 mL of deionized water, followed by the addition of the obtained NCS@MCMB precursor. The suspension was stirred for 20 min,

transferred into a 50 mL Teflon-lined stainless steel auto-clave, and maintained at 160 °C for 12 h. After cooling down to room temperature, the precipitate was collected and washed several times with deionized water and ethanol, and then dried at 60 °C for 24 h in vacuum to yield a sample containing 75% NCS, labeled NCS@MCMB-75%.

For comparison, two additional samples, labeled NCS@MCMB-65% and NCS@MCMB-85%, were synthesized under the same reaction conditions but with NCS percentages of 65% and 85%, respectively. Pure NCS, CoS@MCMB, and NiS@MCMB were also synthesized under the same conditions.

2.2 Material Characterization

The crystalline structure of the samples was identified by X-ray diffraction (XRD) using a Rigaku D/max 2500 V diffractometer (Rigaku, Japan) with Cu K_α radiation ($\lambda = 1.5418$ Å), operating voltage and current of 40 kV and 40 mA, respectively, and 2θ range from 20° to 70°. The morphology was characterized by Sirion 200 scanning electron microscopy (SEM, FEI, USA) and JEM 2100 F transmission electron microscopy (TEM, JEOL, Japan) with operating voltage 200 kV. X-ray photoelectron spectroscopy (XPS) measurements were taken using a Kratos Axis spectrometer (Kratos, Britain) with monochromatic Al K_α radiation (1486.71 eV), operating voltage and current of 15 kV and 10 mA, respectively, and a hemispherical electron energy analyzer. Raman spectra were recorder on an inVia spectrometer (Renishaw, Britain) with a 514 nm excitation source. Nitrogen adsorption/desorption isotherms at 77 K were measured using a Micromeritics Autosorb-iQ2-C instrument (Quantachrome, USA); specific surface areas were estimated by the Brunauer–Emmett–Teller (BET) method. Thermogravimetric analysis (TGA) was performed using Pyris 1 analyzer (PerkinElmer, USA) by heating under air flow from 30 to 900 °C at a rate of 10 °C min^{-1}.

2.3 Electrochemical Measurements

Electrochemical tests were performed on an electrochemical workstation (CHI 760e, Shanghai Chenhua, China), using a 3 M KOH aqueous solution at room temperature. The tests were performed in a three-electrode configuration with Pt foil, Ag/AgCl, and sample-modified nickel foam as

counter, reference, and working electrodes, respectively. To prepare the working electrodes, the samples, acetylene black, and polyvinylidene fluoride (PVDF) were mixed in a 80:10:10 weight ratio in N-methyl-2-pyrrolidone (NMP) to form a slurry, which was pasted uniformly onto Ni foam (1 cm × 4 cm) with a thickness of 2 mm and dried in a vacuum oven at 120 °C for 12 h to remove the solvent. The mass loading of each electrode was about 2.5 mg (pasting surface area: 1 cm × 1 cm), corresponding to an areal mass loading capacity of 2.5 mg cm^{-2}. The specific capacitance (F g^{-1}) and current rate (A g^{-1}) values were calculated based on the total mass of active material. Cyclic voltammetry (CV) measurements were taken from 0 to 0.5 V, at scanning rates from 2 to 100 mV s^{-1}. Galvanostatic charge–discharge (GCD) measurements were taken from 0 to 0.5 V at current densities of 1–10 A g^{-1}. Electrochemical impedance spectroscopy (EIS) measurements were taken by applying an alternate current voltage amplitude of 5 mV in the frequency range from 100 kHz to 0.01 Hz. All electrochemical measurements were taken at room temperature, and the specific capacitance (C) was calculated as $C = (I \times \Delta t)/(\Delta V \times m)$, where m is the mass (g) of active material, I is the constant discharge current (A), ΔV is the applied potential window (V), and t denotes the discharge time (s).

The ASC device was fabricated using active carbon (AC) and the NCS@MCMB composite as the negative and positive electrodes, respectively. The device was fabricated using a CR2016-type coin cell with 3 M KOH solution as the electrolyte and one piece of cellulose paper as the separator. The energy density (E, Wh kg^{-1}) and power density (P, W kg^{-1}) of the NCS@MCMB//AC ASC device were calculated from the equations: $E = CV^2/2$ and $P = E/\Delta t$, respectively, where V is the applied potential and Δt is the discharge time.

3 Results and Discussion

The mechanism of the two-step hydrothermal synthesis of the urchin-like NCS@MCMB composite is schematically illustrated in Fig. 1. First, MCMB was dispersed into a solution containing Ni^{2+} and Co^{2+}. Owing to the negative zeta potential (i.e., -24.9 mV) of MCMB in the solvent (Fig. S1), the metal Ni^{2+} and Co^{2+} cations were electrostatically attracted to the surface of the electronegative MCMB, which promoted the homogeneous nucleation and tight anchoring of the NCS precursors on MCMB in solution. During
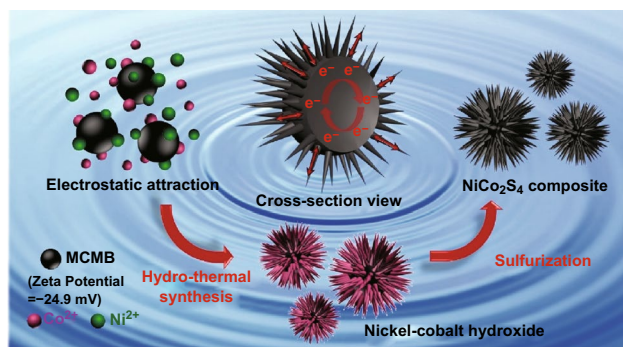
Fig. 1 Schematic illustration of the synthesis procedure of the urchin-like NCS@MCMB composites

the first hydrothermal reaction, nickel–cobalt hydroxides $(NiCo_2(OH)_6)$ crystallized in situ into nanoneedles located on the surface of MCMB, forming a core–shell urchin-like structure. The structure of the NCS@MCMB precursor was well preserved in the subsequent sulfurization during the second hydrothermal reaction, which allowed the transformation of hydroxides into sulfides [49], forming the stable urchin-like NCS@MCMB composite with core–shell structure. The open urchin-like structure enabled each NCS nanoneedle to effectively unfold, facilitating ion transfer

with the electrolyte. At the same time, the MCMB served as a highly conductive electron collector, providing numerous electron transfer pathways. Therefore, the NCS@MCMB composite showed enhanced charge transfer and redox reaction activity, resulting in an increased specific capacitance and high-rate performance of the NCS@MCMB electrode.

The morphology changes occurring during the synthesis process were examined by SEM. Pure MCMB had an ideal spherical morphology, with a rough surface providing abundant adsorption sites (Fig. 2a). Pure NCS synthesized without the support of MCMB appeared as randomly arranged nanoneedles (Fig. 2b). When the NCS nanoneedles were synthesized in the presence of MCMB, their crystallization tended to occur on the MCMB surface, which contributed to the urchin-like arrangement of the nanoneedles. This is confirmed by Fig. 2c, which shows nickel–cobalt hydroxide nanoneedles uniformly anchored on MCMB and forming an urchin-like core–shell structure. The structure of the precursor was well retained after the subsequent sulfurization process, leading to the final urchin-like core–shell structure of NCS@MCMB (Fig. 2d), with a slightly larger size than that of pure MCMB. The energy-dispersive X-ray (EDX) spectrum of a single NCS@MCMB spherical particle in
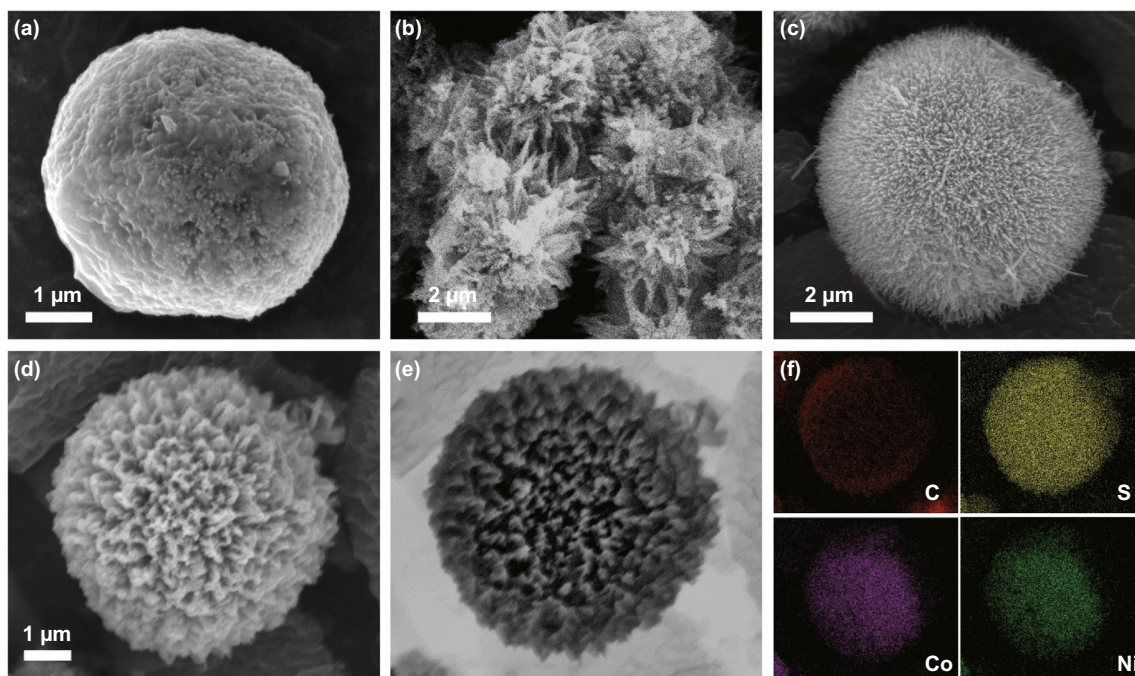

Fig. 2 SEM images of **a** pure MCMB after calcination, **b** pure NCS, **c** NCS@MCMB precursor, and **d** NCS@MCMB composite. **e** SEM backscattered image of an individual NCS@MCMB sphere and **f** corresponding EDX elemental maps of C, S, Co, and Ni

Fig. 2e, f shows that the C, S, Co, and Ni elements were uniformly distributed within the composite, further confirming its composition. Figure S2 displays a SEM image of the cross section of the electrode, revealing that the composite was closely attached to the Ni foam and retained its morphology; the average coating thickness was around 15 μm.

The detailed morphology of the as-synthesized NCS@MCMB composite was further investigated by TEM and high-resolution TEM (HRTEM). The TEM image in Fig. 3a shows that numerous nanoneedles were distributed around the MCMB spheres, consistent with the SEM results. Furthermore, the high-magnification image in Fig. 3b highlights the porous structure of the NCS nanoneedles, which consisted of interconnected ultra-small NCS grains, formed from the anion exchange reaction during the sulfurization process [50]. The HRTEM image in Fig. 3c clearly shows a lattice fringe spacing of 0.54 nm, corresponding to the (111)

plane of the spinel-structured $NiCo_2S_4$ phase. The polycrystalline nature of these NCS nanocrystals was also confirmed by the selected area electron diffraction (SAED) pattern displayed in Fig. 3d. Both SEM and TEM images highlight the open porous structure [50] of the composite, with numerous NCS nanoneedles tightly anchored on the MCMB surface, which is expected to result in a large specific surface area, abundant active sites for redox reactions, and superior electrochemical performances.

The XRD patterns of the NCS@MCMB composite and of the individual component materials are shown in Fig. 4a. The main diffraction peaks at 26.8°, 31.6°, 38.3°, 50.5°, and 55.3° in both NCS@MCMB and NCS alone could be, respectively, indexed to the (220), (311), (400), (511), and (440) planes of the standard spinel-structured $NiCo_2S_4$ (PDF #20-0782), indicating their well-crystallized structure. The EDX analysis (Fig. S3) indicated an Ni:Co:S atomic ratio of
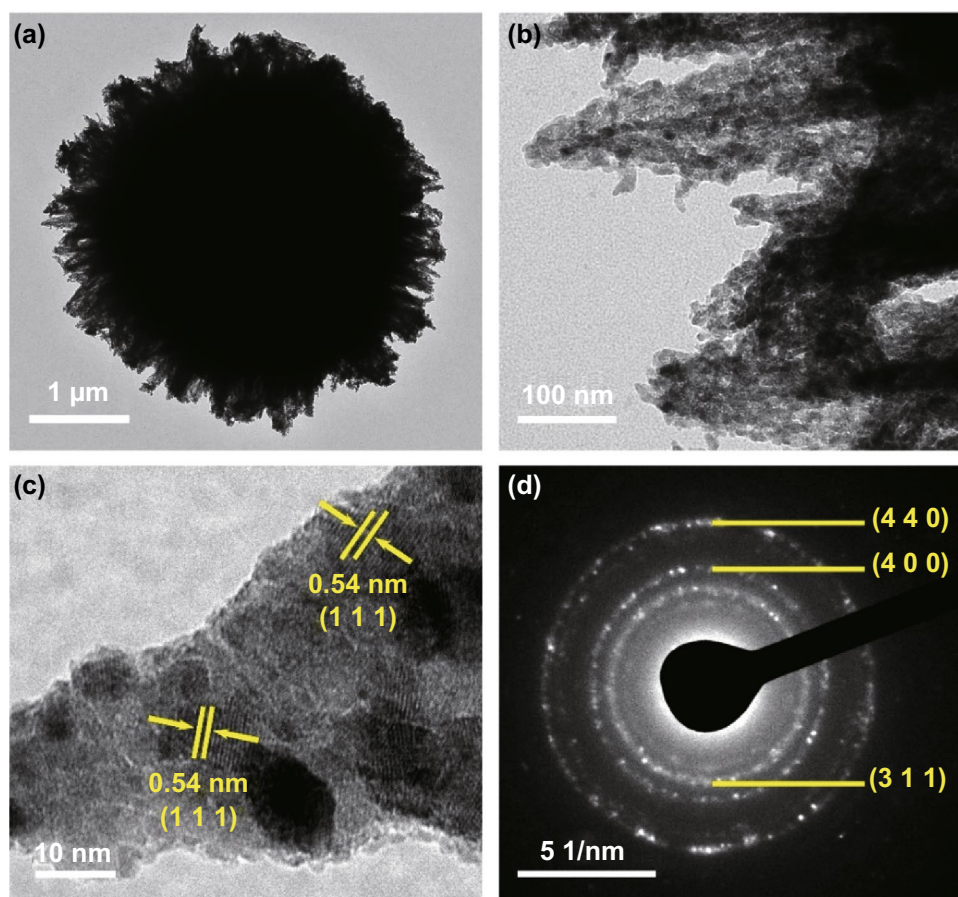

Fig. 3 TEM images of **a** an individual NCS@MCMB sphere and **b** NCS nanoneedles anchored on it. **c** HRTEM image of NCS nanoneedles and **d** corresponding SAED patterns
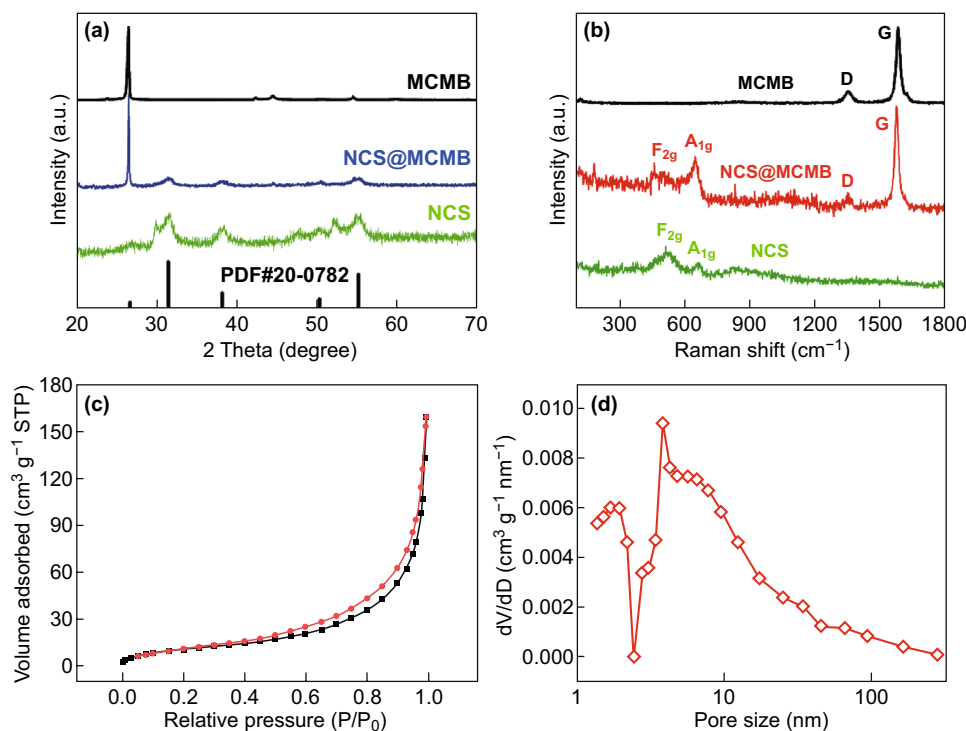
Fig. 4 **a** XRD patterns and **b** Raman spectra of pure MCMB, NCS@MCMB, and pure NCS. **c** Nitrogen adsorption/desorption isotherm and **d** pore size distribution of NCS@MCMB composite

approximately 1:2:4 (14.10:29.28:56.62), consistent with the stoichiometric ratio of NiCo$_2$S$_4$. In addition, the same sharp diffraction peak at 26.5° was found for both pure MCMB and the composite, indicating the successful combination of NCS and MCMB. The structural features of the NCS@MCMB composite were further examined through the Raman spectra as shown in Fig. 4b. Two prominent peaks located at 1350 cm^{-1} (D band) and 1583 cm^{-1} (G band) were observed for both pure MCMB and NCS@MCMB. The D and G bands correspond to the disorder-induced features associated with sp^2-bonded carbon and to the in-plane bond-stretching vibrations of sp^2-hybridized carbon atoms, respectively [51, 52]. The intensity of D band was relatively low, implying a low number of defects in MCMB and a corresponding high conductivity. Furthermore, no obvious shift was observed in the G and D bands of pure MCMB and NCS@MCMB, which highlighted the stability of the MCMB structure after compositing with NCS. In addition, the peaks at 519 and 662 cm^{-1} in NCS and NCS@MCMB corresponded to the F_{2g} and A_{1g} modes of NiCo$_2$S$_4$, respectively [53, 54]. The N$_2$ adsorption–desorption isotherm of the NCS@MCMB composite (Fig. 4c) shows a typical type

IV isotherm with a distinct hysteresis loop in the relative pressure range of 0.4–1.0, as well as a decreasing slope at low relative pressures [55]. The BET specific surface area was calculated to be 69.8 m^2 g^{-1}. Furthermore, the NCS@MCMB composite showed typical pore sizes (Fig. 4d) in the ranges of 1.35–1.93 nm (indicating a small amount of micropores) and 3.8–9.5 nm (corresponding to a large number of mesopores), consistent with the porous structure of the NCS nanoneedles observed in the TEM images. The N$_2$ adsorption–desorption isotherms and pore size distribution of pure NCS and MCMB were also tested and are shown in Fig. S4, which reveals much smaller specific surface areas and higher average pore sizes compared to those of the NCS@MCMB composite. The improved surface area of NCS@MCMB further confirmed the effective unfolding of NCS nanoneedles attached to MCMB, which resulted in an open and porous structure of the composite. Based on the TGA curves in Fig. S5, the full combustion of MCMB and the thermal decomposition of NCS occurred at 900 °C. The weight losses of pure NCS and NCS@MCMB were measured to be about 23% and 39%, respectively. Therefore, the content of MCMB in the NCS@MCMB-75% sample

was calculated to be 21%, essentially in agreement with the expected content.

Detailed insight into the surface electronic states of the NCS@MCMB composite was obtained by XPS measurements; the spectra of all main elements, including C, S, Co, and Ni, are shown in Fig. 5. The C 1*s* spectrum (Fig. 5a) showed four major peaks corresponding to C–C, C=C, C–O, and O=C–O, indicating the presence of abundant oxygen-containing functional groups on the surface of MCMB. The existence of these functional groups played an important role in increasing the wettability of MCMB in the electrolyte and in improving the utilization of the specific surface area of MCMB, which further enhanced the pseudo-capacitive performance and the specific capacitance of the electrode materials. The S 2*p* spectrum (Fig. 5b) showed three peaks at 169.1, 161.4, and 163.0 eV, corresponding to a shake-up satellite as well as to S 2$p_{3/2}$ and S 2$p_{1/2}$ states, respectively. The peak at 162.5 eV was attributed to low-coordinated divalent sulfide ions (S^{2-}) on the surface, while the peak at 163.8 eV corresponded to typical metal–sulfur

(M–S) bonds (Ni–S and Co–S) [29, 56]. The Co 2*p* spectrum (Fig. 5c) showed major peaks located at 782.8/798.8 eV for Co^{2+} and 780.0/795.0 eV for Co^{3+}, with two shake-up satellites at 787.2 and 804.3 eV. The weak satellite peaks suggest that Co^{3+} was the dominant Co state. The Ni 2*p* spectrum (Fig. 5d) showed major peaks located at 855.2/874.6 eV for Ni^{2+} and 858.0/875.8 eV for Ni^{3+}, with two shake-up satellites at 863.6 and 881.6 eV. The intense satellite peaks indicated that most Ni atoms were in the Ni^{2+} state. The coexistence of cations with different electronic states (Co^{3+}/Co^{2+} and Ni^{3+}/Ni^{2+}) was accompanied by the presence of abundant active sites, which is beneficial for energy storage. The XPS results further confirmed the successful preparation of the NCS@MCMB composite.

The electrochemical performances of NCS@MCMB composites with different loading amounts of NCS were evaluated by applying them as electrodes for supercapacitors. Pure NCS and MCMB electrodes were also tested for comparison. Figure 6a shows the CV curves of NCS@MCMB-75%, pure NCS, and MCMB electrodes recorded
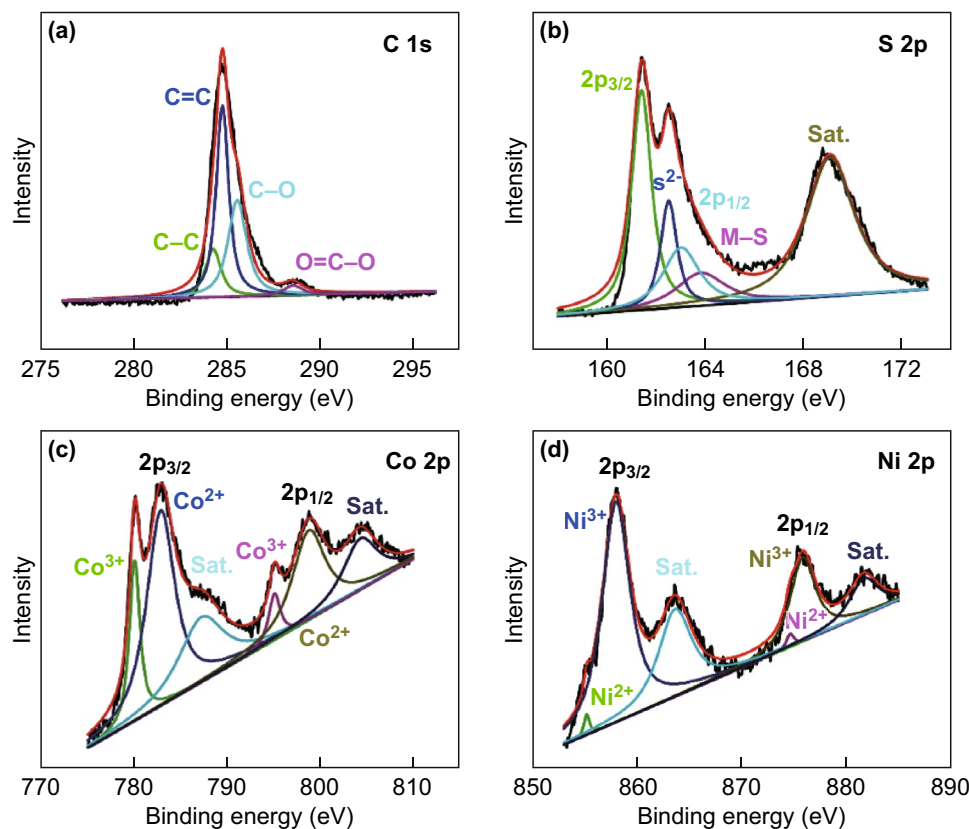

Fig. 5 High-resolution XPS spectra of **a** C 1*s*, **b** S 2*p*, **c** Co 2*p*, and **d** Ni 2*p* levels
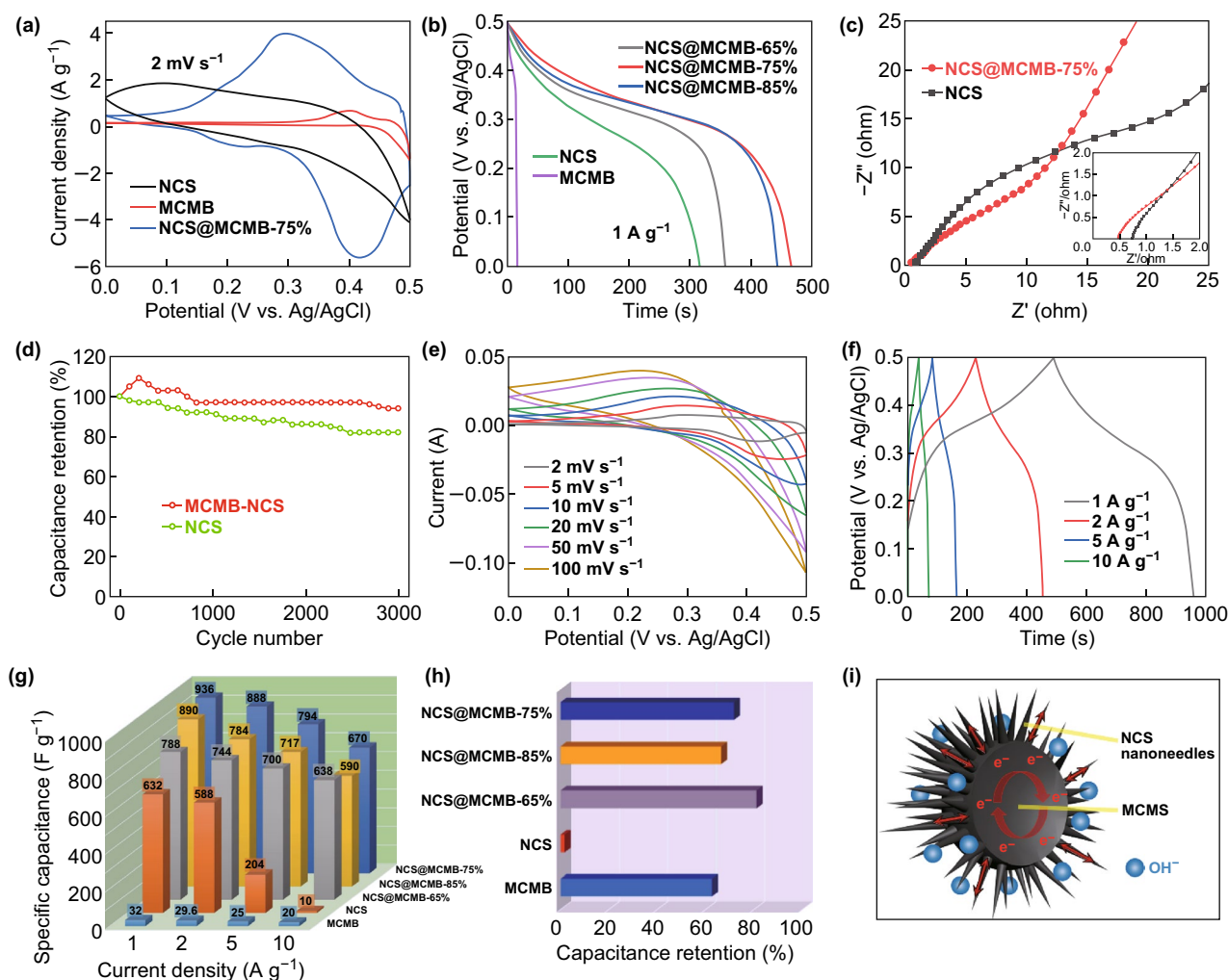
Fig. 6 **a** CV curves at a scanning rate of 2 mV s^{-1}, **b** GCD curves at a current density of 1 A g^{-1}, **c** EIS spectra, and **d** cycling tests of NCS@MCMB and NCS. Typical **e** CV and **f** GCD curves of NCS@MCMB-75%. **g** Specific capacitance and **h** capacitance retention of NCS@MCMB, MCMB, and NCS at increased current densities. **i** Schematic diagrams illustrating the kinetic advantages of the NCS@MCMB composite in electrochemical energy storage

at the scan rate of 2 mV s^{-1}. Among the three electrodes, the MCMB@NCS-75% one exhibited the strongest redox peaks, indicating the occurrence of Faradaic redox processes mainly related to the Co^{2+}/Co^{3+} and Ni^{2+}/Ni^{3+} redox couples [57]. Compared with those of pure NCS, the NCS@MCMB-75% composite presented a higher redox peak current and a larger area under the CV curves, suggesting that MCMB contributes to enhance the electrochemical activity and pseudocapacitive performances. The area under the CV curve suggests that the capacitance contribution from MCMB was negligible. Figure 6b shows the GCD curves of pure NCS, MCMB, and NCS@MCMB electrodes within the potential window of 0–0.5 V at 1 A g^{-1}. Compared with

those of the individual component materials, the longer discharge time in the composites indicates higher specific capacitances. This was attributed to the increased utilization rate of active materials due to the unique urchin-like structure of NCS@MCMB. Moreover, the longest discharge time of the NCS@MCMB-75% electrode reveals that an optimal NCS amount was loaded in this composite, maximizing the positive effects of the highly conductive MCMB to compensate the low capacitance. The resistance characteristics of the NCS@MCMB composite and NCS were determined by examining the Nyquist plots (Fig. 6c) obtained from the EIS measurements. Compared with pure NCS, the composite exhibited a larger slope in the low-frequency region,

along with a smaller semicircle diameter and a lower real axis intercept at high frequencies, revealing lower diffusion resistance (R_w), interfacial charge transfer resistance (R_{ct}), and equivalent series resistance (R_s) values, respectively [37, 58]. Overall, the EIS results reveal the improved electrical conductivity and enhanced Faradaic redox reactions of the NCS@MCMB composite, which are favorable for achieving the excellent rate capability and sustained cycling stability of the electrode.

The long-term cycling performance of the NCS and NCS@MCMB-75% electrodes were investigated at 5 A g^{-1} for 3000 cycles, and the corresponding results are shown in Fig. 6d. The capacitance retention of NCS@MCMB over 3000 cycles was 94%, larger than the 82% value obtained for pure NCS, which highlights an obvious improvement in cycling stability. The cycling stability of NCS@MCMB was also improved with respect to that of previously reported NCS electrodes [59–62], demonstrating its good structural stability during electrochemical reactions. Apart from the high electrical conductivity revealed by the EIS results, the sustained cycling stability of the NCS@MCMB composite also benefitted from the tight integration, better interfacial interaction, and improved electrical contact between NCS nanoneedles and MCMB. In addition, MCMB served as an ideal substrate material to reduce the agglomeration of NCS nanoneedles during the long-term cycling tests, resulting in a highly stable composite structure.

As shown in Fig. 6e, the CV curves of the NCS@ MCMB-75% electrode were further evaluated at different scan rates ranging from 2 to 100 mV s^{-1}, within the potential window of 0–0.5 V. The 50-fold increase in scan rate resulted in the anode peak shifting slightly from 0.29 to 0.23 V, demonstrating the excellent high-rate reversibility of the composite electrode [63, 64]. The obvious redox peaks in the CV curves confirmed the pseudocapacitive behavior of NCS, which was responsible for its large capacitance [62, 65]. Similar Faradaic redox peaks were observed in both NCS@MCMB-65% and NCS@MCMB-85% composites (Fig. S6b, d), which also exhibited more obvious redox peaks compared with those of pure NCS or MCMB (Fig. S7b, d), further confirming the enhanced pseudocapacitive characteristics of NCS@MCMB. The nonlinear trend of the GCD curves at high current densities ranging from 1 to 10 A g^{-1} (Fig. 6f) further confirmed the Faradaic characteristic of NCS@MCMB. The GCD curves presented voltage plateaus at around 0.35 V

consistent with the CV curves, implying the high reversibility of the composite. The specific capacitance values at different current densities and the capacitance retention values (Fig. 6g, h) were calculated from the GCD measurements of various electrodes (Figs. 6f, S6a, c, and S7a, c). Although pure NCS possessed a high capacitance of 632 F g^{-1} at 1 A g^{-1}, this value sharply decreased with the gradual increase in current density (1.6% capacitance retention at 10 A g^{-1}). In contrast, MCMB exhibited a lower specific capacitance (32 F g^{-1} at 1 A g^{-1}) but also an excellent rate performance (62.5% capacitance retention). Therefore, the NCS@MCMB composite exhibited a synergistic effect between the two components, which led to greatly improved capacitance and rate performance. Among the composites with different NCS contents, the NCS@MCMB-75% electrode displayed the highest specific capacitances, with values of 936, 888, 794, and 670 F g^{-1} at current densities of 1, 2, 5, and 10 A g^{-1}, respectively. This indicated that about 71.58% of the specific capacitance was retained after a tenfold increase in current density, indicating excellent rate capability. In contrast, the lower capacitance of NCS@MCMB-85% (890 F g^{-1} at 1 A g^{-1}) might be due to the underutilization of the NCS grains that were not loaded on MCMB. Despite a slightly higher capacitance retention of 80.96% than that of NCS@MCMB-75%, the NCS@MCMB-65% composite displayed a much lower capacitance (788 F g^{-1} at 1 A g^{-1}), due to its lower NCS content. Therefore, we inferred that the NCS@MCMB-75% composite possessed an optimal NCS:MCMB ratio, which achieved a favorable balance between high capacitance and high-rate performance. The superior electrochemical performances of the NCS@MCMB composites originated from their unique urchin-like structure (Fig. 6i). On the one hand, the NCS nanoneedles were sufficiently unfolded to gain full contact with the OH$^-$ groups in the electrolyte, thereby promoting the Faradaic redox processes on the NCS nanoneedles. On the other hand, the highly conductive MCMB served as a substrate to support individual NCS nanoneedles, which greatly enhanced the electron transfer in the composite. The favorable charge transfer in the NCS@ MCMB composite resulted in high specific capacitances, promising high-rate performance, and excellent long-term cycling stability. We also prepared monometallic CoS@ MCMB and NiS@MCMB composites, and their CV and GCD curves are shown in Fig. S8. Both materials showed

smaller capacitances than NCS@MCMB (391 F g^{-1} for CoS@MCMB and 474 F g^{-1} for NiS@MCMB), demonstrating the beneficial effect of bimetallic Ni–Co sulfides.

The stability of the composite structure could be further confirmed by inspecting the morphology after cycling. As shown in Fig. 7a, the SEM image highlights an unchanged urchin-like spherical shape without obvious collapse and aggregation, in good agreement with the TEM image of an individual NCS@MCMB sphere (Fig. 7b). Moreover, the enlarged image of a part of the urchin-like NCS@MCMB sphere (Fig. 7c) shows that each NCS nanoneedle retained their porous and perfect needlelike structure without breaking. These results illustrate the strong interaction between the NCS nanoneedles and MCMB, which allowed the composite to maintain its integrated urchin-like morphology after the long-term cycling process. Moreover, clear lattice fringe spacings were observed at 0.22, 0.27, and 0.28 nm in Fig. 7d, corresponding to the (220), (222), and (311) planes, respectively, indicating that the crystal structure and polycrystalline feature of the NCS nanoneedles did not change during the pseudocapacitive reactions. No obvious peak shift was found in the XPS C 1*s*, S 2*p*, Co 2*p*, and Ni 2*p* spectra after cycling (Fig. S9), further confirming the excellent compositional and structural stability of the composite. The high structural stability of the NCS@MCMB composite was responsible for the excellent cyclic reversibility and high capacitance retention of the electrode.

To further evaluate the potential application of the NCS@MCMB composite, we assembled an asymmetric supercapacitor device with NCS@MCMB as the positive electrode and active carbon as the negative electrode (Fig. 8a). In order to ensure the charge storage balance between the positive and negative electrodes ($Q_+ = Q_-$), the masses of the active materials should follow the equation $(m_-/m_+) = (C_+ \times \Delta V_+)/(C_- \times \Delta V_-)$, where the "+" and "_" subscripts correspond to the positive and negative charge carriers, m is the mass of active material, C is the specific capacitance of the electrode, and ΔV is the potential
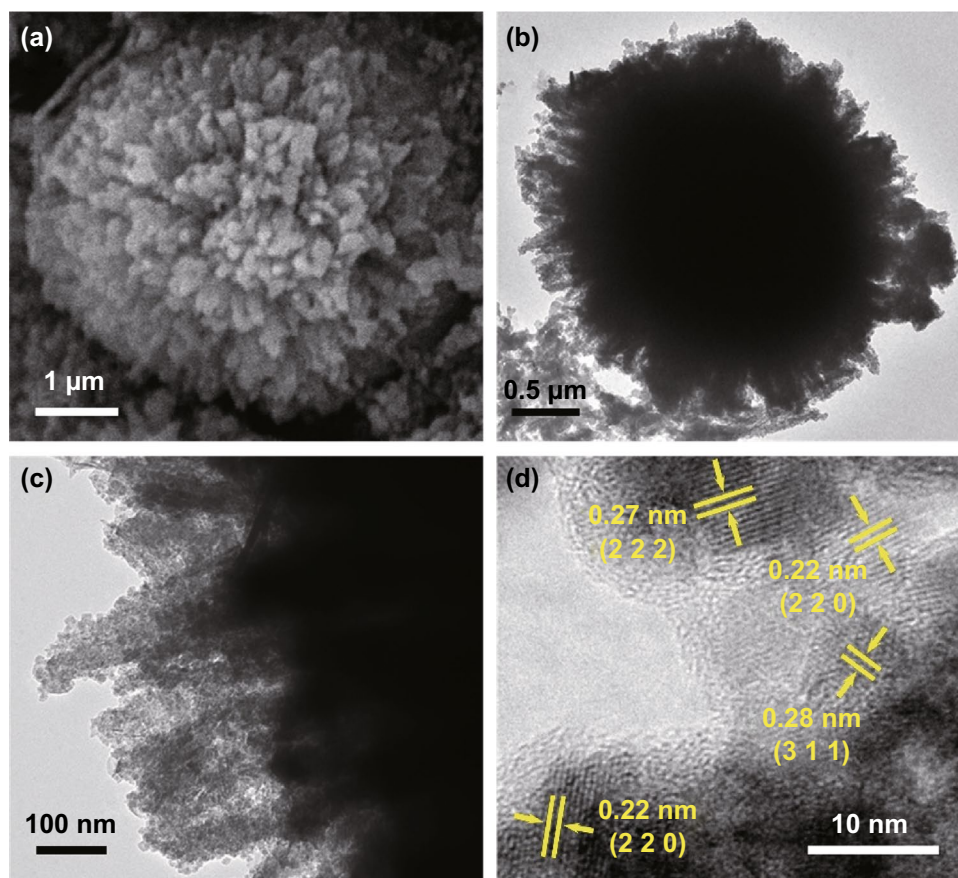

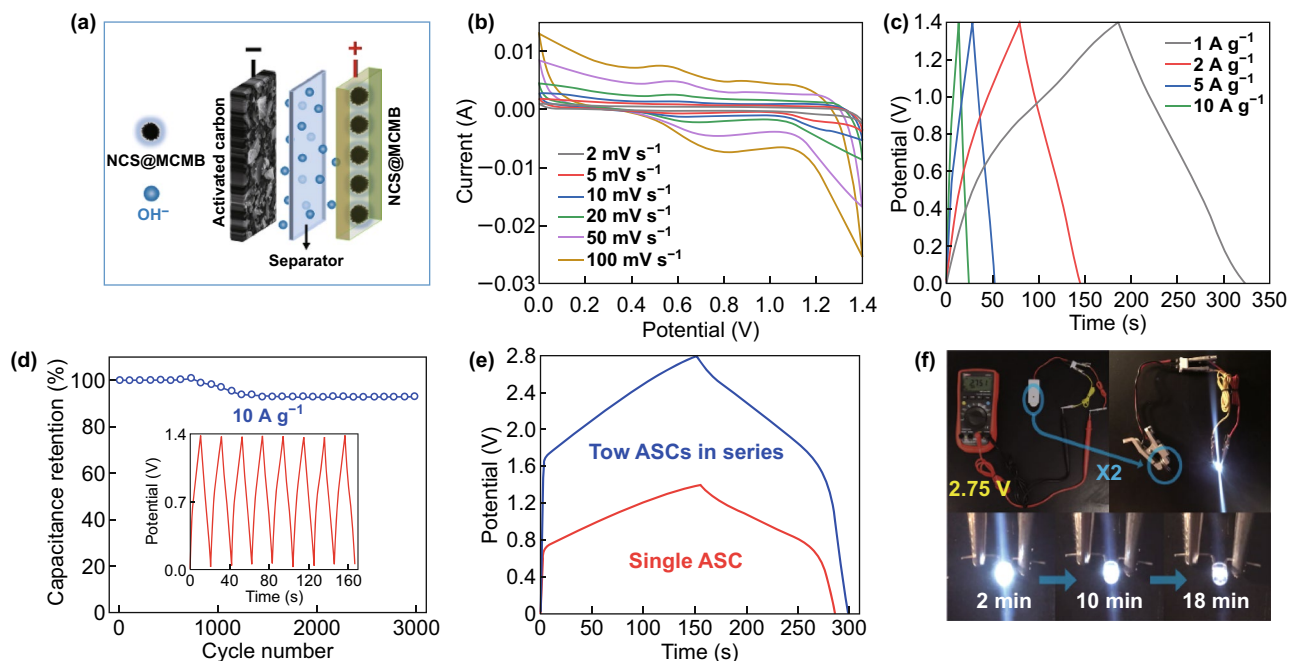**Fig. 7** **a** SEM, **b, c** TEM, and **d** HRTEM images of NCS@MCMB after cycling

Fig. 8 **a** Schematic illustration of the structure of the NCS@MCMB//AC ASC device. **b**, **c** Typical CV and GCD curves of the ASC device. **d** Cycling test of the ASC device at 10 A g^{-1} and GCD curves in the last eight cycles (inset of **d**). **e** GCD curves of single ASC and two ASCs connected in series. **f** Photographs of two ASC devices connected in series, powering a red LED indicator

range for the electrochemical reaction [66]. Based on the 105 F g^{-1} specific capacitance of AC calculated from the GCD curve in Fig. S10a, the optimal NCS@MCMB:AC mass ratio in the NCS@MCMB//AC ASC was calculated to be about 4.5. Figure S10b shows the CV curves of AC and NCS@MCMB electrodes, whose stable voltage windows were identified as −0.9 to 0 V and 0 to 0.5 V, respectively, corresponding to the 0–1.4 V voltage window in the ASC device (Fig. 8b). As shown in Fig. 8b, the CV curve of the ASC device suggests the presence of both electric double-layer capacitance and pseudocapacitance. Similar shapes, without evident distortion, were retained by the CV curves as the scanning rate was increased, indicating excellent capacitive characteristics and rate capability. The GCD curves of the ASC device at current densities ranging from 1 to 10 A g^{-1} (Fig. 8c) showed quasi-triangular shapes with good symmetry, suggesting excellent reversibility and capacitive characteristics. According to the GCD curves, the specific capacitances of the ASC at current densities of 1, 2, 5, and 10 A g^{-1} were calculated to be 97.79, 93.14, 85.71, and 78.57 F g^{-1}, respectively, confirming the excellent capacitive characteristics and rate capability. A reasonable total capacitance

(C_T, 97.79 F g^{-1}) of the ASC device is estimated from Eq. $1/C_T = 1/C_p + 1/C_n$, where C_p and C_n are the capacitances of the positive (936 F g^{-1}) and negative (105 F g^{-1}) electrodes, respectively. Furthermore, the long-term stability was investigated at the current density of 10 A g^{-1} (Fig. 8d). The results reveal a superior cycling stability, with 96.2% capacitance retention after 3000 cycles. The GCD curves of the last eight cycles (shown in the inset of Fig. 8d) remained almost unchanged, which demonstrated an excellent cyclic reversibility. The Ragone plots (energy density vs. power density) shown in Fig. S11 represent important tools for evaluating the potential application of an ASC device. They show that the NCS@MCMB//AC ASC delivered an energy density of 26.62 Wh kg^{-1} at a low power density of 699.98 W kg^{-1} (1 A g^{-1}) and an energy density of 21.39 Wh kg^{-1} at a high power density of 7000 W kg^{-1} (10 A g^{-1}), which are among the best performance reported for ASCs to date. To further demonstrate the excellent performance of the NCS@MCMB composite, two ASC devices were connected in series to power a white light-emitting diode (LED, about 3.0 V). As shown in the GCD curves (Fig. 8e), the operating voltage of the two ASC devices could reach 2.8 V, consistent with

the voltage monitored by a digital multimeter (Fig. 8f), thus achieving the voltage required to power the LED. In fact, as shown in Fig. 8f, after charging for 20 s, the LED was powered for as long as 18 min, further evidencing the excellent performance of the devices and the potential applications of the NCS@MCMB composite.

The outstanding electrochemical performances of the MCMB@NCS composite could be ascribed to its unique microstructure and the synergistic effect of MCMB and NCS. First, the bimetallic sulfides possessed abundant active sites for the Faradaic redox reactions, resulting in a high specific capacitance of the composite. Second, the MCMB component imparted excellent electrical conductivity to the composite, leading to rapid electron transfer and high-rate performance. Third, the composite presented a highly porous structure, which enhanced cationic diffusion in the electrolyte, thereby leading to improved ion transport efficiency. Fourth, the NCS nanoneedles were uniformly anchored on the MCMB surface, which allowed them to be fully unfolded and effectively contribute to the Faradaic redox reactions, thereby leading to a greatly increased utilization ratio of NCS and superior pseudocapacitive characteristics. Moreover, the stable composite structure with a strong NCS-MCMB interaction allowed maintaining a high structural stability during the redox reactions, thereby leading to highly reversible electrochemical reactions and significantly enhanced cycling performance.

4 Conclusions

In summary, a simple two-step hydrothermal strategy was developed to synthesize a NCS@MCMB composite with unique urchin-like core–shell structure, in which bimetallic NCS nanoneedles were uniformly anchored on MCMB. When evaluated as an electrode material for supercapacitors, the unique structure and synergistic effects endowed the composite electrode with a high specific capacitance of 936 F g^{-1} at 1 A g^{-1}, high cyclic stability (96.2% capacitance retention after 3000 cycles), and promising rate capability (670 F g^{-1} at 10 A g^{-1}). An asymmetric supercapacitor was also fabricated, which showed great promise for practical applications in the energy storage field. Moreover, the present fabrication procedure and device architecture could be extended to other active bimetallic and carbonaceous materials and promote future applications in high-performance electrochemical energy storage/conversion devices.

References

1. J.R. Miller, P. Simon, Electrochemical capacitors for energy management. Science **321**(5889), 651–652 (2008). https://doi.org/10.1126/science.1158736
2. P. Simon, Y. Gogotsi, Materials for electrochemical capacitors. Nat. Mater. **7**(11), 845–854 (2008). https://doi.org/10.1038/nmat2297
3. P. Simon, Y. Gogotsi, B. Dunn, Materials science. Where do batteries end and supercapacitors begin? Science **343**(6176), 1210–1211 (2014). https://doi.org/10.1126/science.1249625
4. G. Zhang, H. Liu, J. Qu, J. Li, Two-dimensional layered MoS$_2$: rational design, properties and electrochemical applications. Energy Environ. Sci. **9**(4), 1190–1209 (2016). https://doi.org/10.1039/C5EE03761A
5. S. Li, M. Li, Y. Jiang, W. Kong, K. Jiang, J. Wang, S. Fan, Sulfur nanocrystals confined in carbon nanotube network as a binder-free electrode for high performance lithium sulfur batteries. Nano Lett. **14**(7), 4044–4049 (2014). https://doi.org/10.1021/nl501486n
6. Y. Wang, Y. Song, Y. Xia, Electrochemical capacitors: mechanism, materials, systems, characterization and applications. Chem. Soc. Rev. **45**(21), 5925–5950 (2016). https://doi.org/10.1039/c5cs00580a
7. G. Yu, X. Xie, L. Pan, Z. Bao, Y. Cui, J. Nanoen, Hybrid nanostructured materials for high-performance electrochemical capacitors. Nano Energy **2**(2), 213–234 (2013). https://doi.org/10.1016/j.nanoen.2012.10.006
8. C. Zhou, Y. Zhang, Y. Li, J. Liu, Construction of high-capacitance 3D CoO@polypyrrole nanowire array electrode for aqueous asymmetric supercapacitor. Nano Lett. **13**(5), 2078–2085 (2013). https://doi.org/10.1021/nl400378j

9. J. Jiang, Y. Li, J. Liu, X. Huang, C. Yuan, X.W. Lou, Recent advances in metal oxide-based electrode architecture design for electrochemical energy storage. Adv. Mater. **24**(38), 5166–5180 (2012). https://doi.org/10.1002/adma.201202146

10. J. Liu, J. Jiang, C. Cheng, H. Li, J. Zhang, H. Gong, H.J. Fan, Co_3O_4 nanowire@MnO_2 ultrathin nanosheet core/shell arrays: a new class of high-performance pseudocapacitive materials. Adv. Mater. **23**(18), 2076–2081 (2011). https://doi.org/10.1002/adma.201100058

11. R. Alcantara, F.J. Madrigal, P. Lavela, J.L. Tirado, J.M. Mateos, C. Salazar, R. Stoyanova, E. Zhecheva, Characterisation of mesocarbon microbeads (MCMB) as active electrode material in lithium and sodium cells. Carbon **38**(7), 1031–1041 (2000). https://doi.org/10.1016/S0008-6223(99)00215-8

12. Y. Xu, X. Huang, Z. Lin, X. Zhong, Y. Huang, X. Duan, One-step strategy to graphene/$Ni(OH)_2$ composite hydrogels as advanced three-dimensional supercapacitor electrode materials. Nano Res. **6**(1), 65–76 (2013). https://doi.org/10.1007/s12274-012-0284-4

13. L. Huang, X. Yao, L.Y. Yuan, B. Yao, X. Gao et al., 4-Butyl-benzenesulfonate modified polypyrrole paper for supercapacitor with exceptional cycling stability. Energy Storage Mater. **12**, 191–196 (2018). https://doi.org/10.1016/j.ensm.2017.12.016

14. L. Winkless, Self-assembled supercapacitor wires for e-textiles. Mater. Today **19**(8), 422 (2016). https://doi.org/10.1016/j.mattod.2016.08.014

15. J. Chen, C. Li, G. Shi, Graphene materials for electrochemical capacitors. J. Phys. Chem. Lett. **4**(8), 1244–1253 (2013). https://doi.org/10.1021/jz400160k

16. H. Wang, Y. Liang, T. Mirfakhrai, Z. Chen, H.S. Casalongue, H. Dai, Advanced asymmetrical supercapacitors based on graphene hybrid materials. Nano Res. **4**(8), 729–736 (2011). https://doi.org/10.1007/s12274-011-0129-6

17. X. Li, B. Wei, Supercapacitors based on nanostructured carbon. Nano Energy **2**(2), 159–173 (2013). https://doi.org/10.1016/j.nanoen.2012.09.008

18. K. Wang, H. Wu, Y. Meng, Z. Wei, Conducting polymer nanowire arrays for high performance supercapacitors. Small **10**(1), 14–31 (2014). https://doi.org/10.1002/smll.201301991

19. X.C. Dong, Y. Zhang, L. Li, H. Su, H. Wei, Binary metal oxide: advanced energy storage materials in supercapacitors. J. Mater. Chem. A **3**(1), 43–59 (2014). https://doi.org/10.1039/c4ta04996a

20. Q. Liao, N. Li, S. Jin, G. Yang, C. Wang, All-solid-state symmetric supercapacitor based on Co_3O_4 nanoparticles on vertically aligned graphene. ACS Nano **9**(5), 5310–5317 (2015). https://doi.org/10.1021/acsnano.5b00821

21. H. Liang, Z. Wei, J. Xiang, H. Xu, G. Li, Y. Huang, Hierarchical core-shell $NiCo_2O_4$@$NiMoO_4$ nanowires grown on carbon cloth as integrated electrode for high-performance supercapacitors. Sci. Rep. **6**, 31465 (2016). https://doi.org/10.1038/srep31465

22. L. Huang, D. Chen, Y. Ding, S. Feng, Z.L. Wang, M. Liu, Nickel-cobalt hydroxide nanosheets coated on $NiCo_2O_4$ nanowires grown on carbon fiber paper for high-performance pseudocapacitors. Nano Lett. **13**(7), 3135–3139 (2013). https://doi.org/10.1021/nl401086t

23. T. Liu, L.Y. Zhang, W. You, J.G. Yu, Core–shell nitrogen-doped carbon hollow spheres/Co_3O_4 nanosheets as advanced electrode for high-performance supercapacitor. Small **14**(12), 1702407 (2017). https://doi.org/10.1002/smll.201702407

24. M.S. Balogun, Y.C. Huang, W.T. Qiu, H. Yang, H.B. Ji, Y.X. Tong, Updates on the development of nanostructured transition metal nitrides for electrochemical energy storage and water splitting. Mater. Today **20**(8), 425–451 (2017). https://doi.org/10.1016/j.mattod.2017.03.019

25. Y.M. Chen, Z. Li, X.W. Lou, General formation of $M_xCo_{3−x}S_4$ (M = Ni, Mn, Zn) hollow tubular structures for hybrid supercapacitors. Angew. Chem. Int. Ed. **127**(36), 10667–10670 (2015). https://doi.org/10.1002/anie.201504349

26. X.Y. Yu, L. Yu, X.W. Lou, Metal sulfide hollow nanostructures for electrochemical energy storage. Adv. Energy Mater. **6**(3), 1501333 (2016). https://doi.org/10.1002/aenm.201501333

27. M.R. Gao, Y.F. Xu, J. Jiang, S.H. Yu, Nanostructured metal chalcogenides: synthesis, modification, and applications in energy conversion and storage devices. Chem. Soc. Rev. **42**(7), 2986–3017 (2013). https://doi.org/10.1039/c2cs35310e

28. S. Peng, L. Li, C. Li, H. Tan, R. Cai, H. Yu, S. Mhaisalkar, M. Srinivasan, S. Ramakrishna, Q. Yan, In situ growth of $NiCo_2S_4$ nanosheets on graphene for high-performance supercapacitors. Chem. Commun. **49**(86), 10178–10180 (2013). https://doi.org/10.1039/C3CC46034G

29. H. Chen, J. Jiang, L. Zhang, H. Wan, T. Qi, D. Xia, Highly conductive $NiCo_2S_4$ urchin-like nanostructures for high-rate pseudocapacitors. Nanoscale **5**(19), 8879–8883 (2013). https://doi.org/10.1039/C3NR02958A

30. J. Xiao, L. Wan, S. Yang, F. Xiao, S. Wang, Design hierarchical electrodes with highly conductive $NiCo_2S_4$ nanotube arrays grown on carbon fiber paper for high-performance pseudocapacitors. Nano Lett. **14**(2), 831 (2014). https://doi.org/10.1021/nl404199v

31. W. Du, Z. Wang, Z. Zhu, S. Hu, X. Zhu, Y. Shi, H. Pang, X. Qian, Facile synthesis and superior electrochemical performances of $CoNi_2S_4$/graphene nanocomposite suitable for supercapacitor electrodes. J. Mater. Chem. A **2**(25), 9613–9619 (2014). https://doi.org/10.1039/c4ta00414k

32. L. Huang, D.C. Chen, Y. Ding, Z.L. Wang, Z.Z. Zeng, M.L. Liu, Hybrid composite $Ni(OH)_2$@$NiCo_2O_4$ grown on carbon fiber paper for high-performance supercapacitors. ACS Appl. Mater. Interfaces **5**(31), 11159–11162 (2013). https://doi.org/10.1021/am403367u

33. T. Liu, C.J. Jiang, B. Cheng, W. You, J.G. Yu, Hierarchical NiS/N-doped carbon composite hollow spheres with excellent supercapacitor performance. J. Mater. Chem. A **5**(40), 21257–21265 (2017). https://doi.org/10.1039/C7TA06149H

34. H. Hu, B.Y. Guan, X.W. Lou, Construction of complex CoS hollow structures with enhanced electrochemical properties for hybrid supercapacitors. Chem **1**(1), 102–113 (2016). https://doi.org/10.1016/j.chempr.2016.06.001

35. C.Y. Chen, Z.Y. Shih, Z. Yang, H.T. Chang, Carbon nanotubes/cobalt sulfide composites as potential high-rate and high-efficiency supercapacitors. J. Power Sources **215**, 43–47 (2012). https://doi.org/10.1016/j.jpowsour.2012.04.075

36. L. Shen, J. Wang, G. Xu, H. Li, H. Dou, X. Zhang, $NiCo_2S_4$ nanosheets grown on nitrogen-doped carbon foams as an advanced electrode for supercapacitors. Adv. Energy Mater. **5**(3), 1400977 (2015). https://doi.org/10.1002/aenm.201400977

37. W. He, C. Wang, H. Li, X. Deng, X. Xu, T. Zhai, Ultrathin and porous $Ni_3S_2/CoNi_2S_4$ 3D-network structure for superhigh energy density asymmetric supercapacitors. Adv. Energy Mater. **7**(21), 1700983 (2017). https://doi.org/10.1002/aenm.201700983

38. C.Z. Wei, N.N. Zhan, J. Tao, S.S. Pang, L.P. Zhang, C. Cheng, D.J. Zhang, Synthesis of hierarchically porous $NiCo_2S_4$ core-shell hollow spheres via self-template route for high performance supercapacitors. Appl. Surf. Sci. **453**, 288–296 (2018). https://doi.org/10.1016/j.apsusc.2018.05.003

39. X. Xiong, G. Waller, D. Ding, D. Chen, B. Rainwater, B. Zhao, Z. Wang, M. Liu, Controlled synthesis of $NiCo_2S_4$ nanostructured arrays on carbon fiber paper for high-performance pseudocapacitors. Nano Energy **16**, 71–80 (2015). https://doi.org/10.1016/j.nanoen.2015.06.018

40. C. Liu, C. Li, K. Ahmed, W. Wang, I. Lee, F. Zaera, C.S. Ozkan, M. Ozkan, Scalable, binderless, and carbonless hierarchical ni nanodendrite foam decorated with hydrous ruthenium dioxide for 1.6 v symmetric supercapacitors. Adv. Mater. Interfaces **3**(6), 1500503 (2016). https://doi.org/10.1002/admi.201500503

41. L. Zhang, L. Zuo, W. Fan, T. Liu, $NiCo_2S_4$ nanosheets grown on 3D networks of nitrogen-doped graphene/carbon nanotubes: advanced anode materials for lithium-ion batteries. ChemElectroChem **3**(9), 1384–1391 (2016). https://doi.org/10.1002/celc.201600183

42. J.B. Wu, X. Gao, H.M. Yu, T.P. Ding, Y.X. Yan et al., A scalable free-standing V_2O_5/CNT film electrode for supercapacitors with a wide operation voltage (1.6 V) in an aqueous electrolyte. Adv. Funct. Mater. **26**(33), 6114–6120 (2016). https://doi.org/10.1002/adfm.201601811

43. Y.T. Luan, H.N. Zhang, F. Yang, J. Yan, K. Zhu et al., Rational design of $NiCo_2S_4$ nanoparticles @ N-doped CNT for hybrid supercapacitor. Appl. Surf. Sci. **447**, 165–172 (2018). https://doi.org/10.1016/j.apsusc.2018.03.236

44. N.N. Wang, Y.J. Wang, S.Z. Cui, H.W. Hou, L.W. Mi, W.H. Chen, A hollow tube-on-tube architecture of carbon-tube-supported nickel cobalt sulfide nanotubes for advanced supercapacitors. ChemNanoMat **3**(4), 269–276 (2017). https://doi.org/10.1002/cnma.201700016

45. D. Bai, F. Wang, J. Lv, F. Zhang, S. Xu, Triple-confined well-dispersed biactive $NiCo_2S_4/Ni_{0.96}S$ on graphene aerogel for high-efficiency lithium storage. ACS Appl. Mater. Interfaces **8**(48), 32853–32861 (2016). https://doi.org/10.1021/acsami.6b11389

46. P. Shen, H.T. Zhang, S.J. Zhang, L.F. Fei, Fabrication of completely interface-engineered $Ni(OH)_2$/rGO nanoarchitectures for high-performance asymmetric supercapacitors. Appl. Surf. Sci. **460**, 65–73 (2018). https://doi.org/10.1016/j.apsusc.2017.09.145

47. T.H. Yao, X. Guo, S.C. Qin, F.Y. Xia, Q. Li, Y.L. Li, Q. Chen, J.S. Li, D.Y. He, Effect of rGO coating on interconnected Co_3O_4 nanosheets and improved supercapacitive behavior of Co_3O_4/rGO/NF architecture. Nano-Micro Lett. **9**(4), 38 (2017). https://doi.org/10.1007/s40820-017-0141-9

48. D.L. Li, Y.N. Gong, M.S. Wang, C.X. Pan, Preparation of sandwich-like $NiCo_2O_4$/rGO/NiO heterostructure on nickel foam for high-performance supercapacitor electrodes. Nano-Micro Lett. **9**(2), 16 (2017). https://doi.org/10.1007/s40820-016-0117-1

49. X. Liu, F. Zou, K. Liu, Z. Qiang, C.J. Taubert, P. Ustriyana, B.D. Vogt, Y. Zhu, A binary metal organic frameworks derived hierarchical hollow Ni_3S_2/Co_9S_8/N-doped carbon composite with superior sodium storage performance. J. Mater. Chem. A **5**(23), 11781–11787 (2017). https://doi.org/10.1039/C7TA00201G

50. C.W. Kung, H.W. Chen, C.Y. Lin, K.C. Huang, R. Vittal, K.C. Ho, CoS acicular nanorod arrays for the counter electrode of an efficient dye-sensitized solar cell. ACS Nano **6**(8), 7016 (2012). https://doi.org/10.1021/nn302063s

51. X. Xie, L. Gao, Characterization of a manganese dioxide/carbon nanotube composite fabricated using an in situ coating method. Carbon **45**(12), 2365–2373 (2007). https://doi.org/10.1016/j.carbon.2007.07.014

52. B. Pandit, B.R. Sankapal, Highly conductive energy efficient electroless anchored silver nanoparticles on mwcnts as supercapacitive electrode. New J. Chem. **41**(19), 10808–10814 (2017). https://doi.org/10.1039/C7NJ01792H

53. J. Yang, M. Ma, C. Sun, Y. Zhang, W. Huang, X. Dong, Hybrid $NiCo_2S_4$@MnO_2 heterostructures for high-performance supercapacitor electrodes. J. Mater. Chem. A **3**(3), 1258–1264 (2014). https://doi.org/10.1039/C4TA05747C

54. J.H. Zhong, A.L. Wang, G.R. Li, J.W. Wang, Y.N. Ou, Y.X. Tong, $Co_3O_4/Ni(OH)_2$ composite mesoporous nanosheet networks as a promising electrode for supercapacitor applications. J. Mater. Chem. **22**(12), 5656–5665 (2012). https://doi.org/10.1039/C2JM15863A

55. W. Liu, M. Ulaganathan, I. Abdelwahab, X. Luo, Z. Chen, S.T. Rong, X. Wang, Y. Liu, D. Geng, Y. Bao, Two-dimensional polymer synthesized via solid-state polymerization for high-performance supercapacitors. ACS Nano **12**(1), 852–860 (2017). https://doi.org/10.1021/acsnano.7b08354

56. H. Chen, J. Jiang, Y. Zhao, L. Zhang, D. Guo, D. Xia, One-pot synthesis of porous nickel cobalt sulphides: tuning the composition for superior pseudocapacitance. J. Mater. Chem. A **3**(1), 428–437 (2014). https://doi.org/10.1039/c4ta04420g

57. H. Wan, J. Jiang, J. Yu, K. Xu, L. Miao, L. Zhang, H. Chen, Y. Ruan, $NiCo_2S_4$ porous nanotubes synthesis via sacrificial templates: high-performance electrode materials of supercapacitors. CrystEngComm **15**(38), 7649–7651 (2013). https://doi.org/10.1039/C3CE41243A

58. J. Zhu, S. Tang, J. Wu, X. Shi, B. Zhu, X. Meng, Wearable high-performance supercapacitors based on silver-sputtered

textiles with $FeCo_2S_4$–$NiCo_2S_4$ composite nanotube-built multitripod architectures as advanced flexible electrodes. Adv. Energy Mater. **7**(2), 1601234 (2017). https://doi.org/10.1002/aenm.201601234

59. Y.M. Fan, Y.C. Liu, X.B. Liu, Y.N. Liu, L.Z. Fan, Hierarchical porous $NiCo_2S_4$-rGO composites for high-performance supercapacitors. Electrochim. Acta **249**, 1–8 (2017). https://doi.org/10.1016/j.electacta.2017.07.175

60. X.L. Ning, F. Li, Y. Zhou, Y.E. Miao, C. Wei, T.X. Liu, Confined growth of uniformly dispersed $NiCo_2S_4$ nanoparticles on nitrogen-doped carbon nanofibers for high-performance asymmetric supercapacitors. Chem. Eng. J. **328**, 599–608 (2017). https://doi.org/10.1016/j.cej.2017.07.062

61. Y.H. Xiao, D.C. Su, X.Z. Wang, L.M. Zhou, S.D. Wu, F. Li, S.M. Fang, In situ growth of ultradispersed $NiCo_2S_4$ nanoparticles on graphene for asymmetric supercapacitors. Electrochim. Acta **176**, 44–50 (2015). https://doi.org/10.1016/j.electacta.2015.06.128

62. T. Peng, Z.Y. Qain, J. Wang, D.L. Song, J.Y. Liu, Q. Liu, P. Wang, Construction of mass-controllable mesoporous $NiCo_2S_4$ electrodes for high performance supercapacitors. J. Mater. Chem. A **2**(45), 19376–19382 (2014). https://doi.org/10.1039/c4ta04246h

63. G.Q. Zhang, H.B. Wu, H.E. Hoster, M.B. Chan-Park, X.W. Lou, Single-crystalline $NiCo_2O_4$ nanoneedle arrays grown on conductive substrates as binder-free electrodes for high-performance supercapacitors. Energy Environ. Sci. **5**(11), 9453–9456 (2012). https://doi.org/10.1039/c2ee22572g

64. Y. Xu, Z. Lin, X. Huang, Y. Wang, Y. Huang, X. Duan, Functionalized graphene hydrogel-based high-performance supercapacitors. Adv. Mater. **25**(40), 5779–5784 (2013). https://doi.org/10.1002/adma.201301928

65. B.Y. Guan, L. Yu, X. Wang, S.Y. Song, X.W. Lou, Formation of onion-like $NiCo_2S_4$ particles via sequential ion-exchange for hybrid supercapacitors. Adv. Mater. **29**(6), 1605051 (2016). https://doi.org/10.1002/adma.201605051

66. J. Zhu, J. Jiang, Z. Sun, J. Luo, Z. Fan, X. Huang, H. Zhang, T. Yu, 3D carbon/cobalt-nickel mixed-oxide hybrid nanostructured arrays for asymmetric supercapacitors. Small **10**(14), 2937–2945 (2014). https://doi.org/10.1002/sml.201302937